

Three-dimensional Conditional Diffusion Models for Cosmological 21 cm Lightcone Emulation

BIN XIA (夏斌) ¹ AND JOHN H. WISE ¹

¹*Center for Relativistic Astrophysics, School of Physics, Georgia Institute of Technology, Atlanta, GA 30332, USA*

ABSTRACT

We investigate conditional diffusion modeling for three-dimensional 21 cm lightcone emulation, focusing on cubes with a sky-plane size of 64×64 and a line-of-sight depth up to 1024 cells. Relative to earlier 2D studies, the 3D setting is substantially harder because memory limits enforce very small micro-batches while the underlying voxel distribution is highly skewed and long tailed. We perform controlled comparisons across preprocessing choices, dynamic-range compression settings, architecture depth, and training duration using 25,600 training lightcones and validation ensembles at fixed parameter points. For validation, each reference parameter point contains 800 21cmFAST realizations with independent initial conditions, and we use 800 samples per model and per reference set for the reported ensemble comparisons. We evaluate generated lightcones with complementary diagnostics in both image and summary-statistic spaces: brightness-temperature slices, the global signal, the power spectrum, and reduced scattering coefficients. Across the tested configurations, preprocessing is the dominant factor governing stable training and the resulting physical fidelity. Among the configurations explored here, Yeo–Johnson preprocessing combined with moderate amplitude compression gives the most consistently favorable trade-off, with the strongest quantitative support coming from rankings based on the standard-deviation-normalized mean absolute error (MAE_{std}) of the global signal and qualitatively compatible behavior in the complementary diagnostics. At the same time, visually plausible 3D samples still retain measurable biases in two-point and higher-order statistics. We therefore view the present work as a simulation-level baseline for three-dimensional 21 cm emulation and for future studies that incorporate more realistic observational effects.

Keywords: cosmology: theory — dark ages, reionization, first stars — methods: numerical — methods: statistical — radio lines: general

1. INTRODUCTION

The redshifted 21 cm signal from the hyperfine transition of neutral hydrogen is a leading probe of Cosmic Dawn and the Epoch of Reionization (EoR; R. Barkana & A. Loeb 2001; M. F. Morales & J. S. B. Wyithe 2010; J. R. Pritchard & A. Loeb 2012). In the redshift range $6 \lesssim z \lesssim 30$, the signal traces the thermal and ionization state of the intergalactic medium and therefore encodes the impact of the first stars, galaxies, and X-ray sources. Its mean evolution and spatial fluctuations are sensitive to both source physics and large-scale structure, making 21 cm tomography a high-information observable.

A broad observational program is aimed at this regime, including the Low Frequency Array (LOFAR), the Murchison Widefield Array (MWA), the Hydrogen

Epoch of Reionization Array (HERA), and the future Square Kilometre Array (SKA) (M. P. van Haarlem et al. 2013; S. J. Tingay et al. 2013; L. Koopmans et al. 2015; D. R. DeBoer et al. 2017). Recent HERA upper limits and astrophysical constraints illustrate the broader shift from forecasting toward data-driven inference (Z. Abdurashidova et al. 2022a,b). Interpreting future imaging data will therefore require forward models that are both fast and physically reliable across broad astrophysical parameter spaces.

Semi-numerical simulations such as 21cmFAST are widely used to generate target distributions for such analyses (A. Mesinger et al. 2011; B. Greig & A. Mesinger 2018). However, large simulation campaigns remain expensive when repeated realizations, parameter sweeps, or downstream simulation-based inference are required. This has motivated growing interest in machine-learning emulators for 21 cm cosmology.

Machine learning has already been applied to parameter inference from tomographic data, lightcone compression, foreground-affected reconstruction, and fast sample generation (D. Prelogović et al. 2021; S. Gagnon-Hartman et al. 2021; P. Villanueva-Domingo & F. Villaescusa-Navarro 2021; X. Zhao et al. 2022). Emulators based on generative adversarial networks (GANs) have also been explored for 21 cm data products (I. J. Goodfellow et al. 2014; F. List & G. F. Lewis 2020; S. Andrianomena et al. 2022; K. Diao & Y. Mao 2023), but these models remain sensitive to training instability, partial mode collapse, and preprocessing choices. More recently, two related developments have sharpened the context for the present work. First, studies of 21 cm summary statistics have shown that different statistics capture complementary information and that wavelet-scattering-based summaries can outperform power-spectrum-only approaches in some settings (S. Cheng et al. 2020; X. Zhao et al. 2024; D. Prelogović & A. Mesinger 2024). Second, generative modeling in cosmology has begun moving from 2D images toward higher-dimensional fields, including 3D conditional diffusion and alternative 21 cm lightcone emulation strategies (A. Rouhiainen et al. 2024; K. Diao & Y. Mao 2025; I. Hothi et al. 2026).

Diffusion models provide a competitive alternative for high-dimensional generative modeling (J. Ho et al. 2020; P. Dhariwal & A. Nichol 2021). In particular, X. Zhao et al. (2023) showed that conditional diffusion models can generate 21 cm images with promising fidelity in two dimensions, while also emphasizing the importance of distribution-level validation using scattering-based summary statistics and Fisher forecasts. That work motivates a natural next question: can conditional diffusion models remain useful when the target changes from 2D slices to full 3D lightcones?

This dimensional change is not merely cosmetic. Adding an extra dimension to the lightcones increases memory cost, forces small micro-batches, amplifies optimization noise, and makes transform-space distortions more consequential after inversion back to physical units. It also raises the standard for evaluation. A model may generate visually plausible slices while still retaining measurable biases in the global signal, the power spectrum, or higher-order morphology.

In this paper, we address three main questions. First, can conditional diffusion remain stable and useful with the substantially harder 3D lightcone data? Second, which preprocessing and dynamic range control choices are most important for stable training? Third, what levels of physical fidelity are recovered across a hierarchy of diagnostics probing mean evolution, two-point struc-

ture, and higher-order non-Gaussian morphology? We will show that the answer is not captured by image inspection alone. Across the tested configurations, the most favorable behavior arises only after explicit control of transformed-space skewness and dynamic range, and the achieved fidelity follows a clear hierarchy: the agreement is strongest in the global signal, weaker in the power spectrum, and weakest in higher-order scattering statistics.

The remainder of this paper is organized as follows. Section 2 summarizes the physical and methodological background, emphasizing the morphology of the 21 cm signal and why three-dimensional conditional diffusion is more challenging than the two-dimensional setting. Section 3 describes the simulation data, conditioning parameters, validation design, diffusion architecture, preprocessing pipeline, and evaluation protocol. Section 4 presents the hyperparameter sweep, identifies the preferred preprocessing and dynamic range control choices, and examines the representative 3D model across image-space and summary-statistic diagnostics. Section 5 discusses what the experiments demonstrate, what limitations remain, and what is required before such emulators can be used in survey-facing inference pipelines. Section 6 summarizes the main conclusions and outlines the role of this work as a simulation-level baseline for future 3D 21 cm emulator studies.

2. PHYSICAL AND METHODOLOGICAL BACKGROUND

2.1. 21 cm Morphology and Non-Gaussian Structure

The redshifted 21 cm signal provides a tomographic view of the thermal and ionization history of the intergalactic medium prior to cosmic reionization. Its morphology is shaped by several coupled physical processes, including density evolution, radiative coupling, gas heating, and reionization. After thermal decoupling from the cosmic microwave background (CMB), the gas cools adiabatically and can produce a 21 cm absorption signal. Once the first luminous sources appear, Ly α coupling drives the spin temperature toward the gas temperature, strengthening the absorption feature, while subsequent X-ray heating can move the signal into emission. During reionization, ionized bubbles expand and suppress the 21 cm brightness temperature over progressively larger regions until most hydrogen becomes ionized (R. Barkana & A. Loeb 2001; J. R. Pritchard & A. Loeb 2012).

These processes imprint structure on multiple physical scales and generate strongly non-Gaussian spatial patterns. In some regions of parameter space, the 21 cm field remains close to a Gaussian-like density field, whereas in others it develops prominent bubble morphol-

ogy, sharp ionization boundaries, and strongly nonlinear contrasts. This combination of large-scale evolution and non-Gaussian structure is precisely what makes 21 cm tomography scientifically powerful, but it also makes emulation demanding: visually plausible samples must reproduce not only mean trends but also morphology-sensitive summaries (X. Zhao et al. 2023).

2.2. Why 3D Conditional Diffusion Is Harder Than 2D

Prior 2D diffusion studies considered conditional generation of 64×64 21 cm images and showed that diffusion-based generation is viable for 21 cm data (X. Zhao et al. 2023). In the 3D lightcone setting studied here, however, transformed-space behavior and dynamic-range control become much more consequential because memory limits force very small micro-batches and amplify optimization noise. The present problem is harder for three coupled reasons.

First, the computational burden grows sharply. Full-resolution 3D lightcone training must contend with strong GPU-memory limitations, small micro-batches, and large training I/O. Second, those computational limits interact with the statistics of the data: heavy-tailed voxel distributions, strong skewness, and inverse-transform distortions become harder to control when optimization noise is amplified by small effective batch sizes. Third, evaluation becomes more demanding. A model can reproduce the broad visual progression of slices while still failing to match lower-order or higher-order summary statistics. These coupled effects motivate the normalization-centered and diagnostic-centered study developed below.

3. METHODS

3.1. Data, Conditioning, and Validation Design

Our target field is the differential 21 cm brightness temperature relative to the CMB,

$$T_{21}(\mathbf{x}, z) = \tilde{T}_{21}(z) x_{\text{HI}}(\mathbf{x}) [1 + \delta(\mathbf{x})] \left(1 - \frac{T_\gamma}{T_S}\right), \quad (1)$$

where $\tilde{T}_{21}(z) = 27(\Omega_b h^2 / 0.023) \sqrt{(0.15 / \Omega_m h^2)(1+z)/10}$ is the redshift-dependent brightness-temperature normalization in units of mK. x_{HI} is the neutral hydrogen fraction, δ is the matter overdensity, T_γ is the CMB temperature, and T_S is the hydrogen spin temperature (S. R. Furlanetto et al. 2006). In the reionization-focused regime considered here, we adopt the standard high spin temperature approximation $T_S \gg T_\gamma$, so the signal primarily traces the evolving ionization and density structure.

Our training dataset has a shape of (25600, 64, 64, 1024) for the 25600 3D lightcones and

(25600, 2) for the conditioning parameters. The corresponding lightcones span 2048 cMpc (comoving megaparsecs) along the line of sight, with a redshift range $z \in [7.51, 20.95]$ and comoving distance range [8.973, 11.021] cGpc. Each voxel therefore corresponds to 2 cMpc along the line of sight, while the transverse dimensions each span 128 cMpc. The conditioning variables are $(\log_{10} T_{\text{vir}}, \zeta)$, where T_{vir} is the minimum virial temperature of halos capable of hosting ionizing sources and ζ is the ionizing efficiency, which controls the number of ionizing photons produced per collapsed baryon. In our training set, $\log_{10} T_{\text{vir}} \in [4, 6]$ and $\zeta \in [10, 250]$. Following X. Zhao et al. (2023), these two parameters are chosen because they capture dominant astrophysical variation in the 21 cm signal while keeping the conditional problem tractable.

The training parameter points are drawn with Latin hypercube sampling across the target parameter space, with one simulated lightcone for each parameter pair. This design is chosen to maximize parameter space coverage at fixed simulation cost. The cosmological parameters are fixed to $(\Omega_m, \Omega_b, n_s, \sigma_8, h) = (0.310, 0.0490, 0.967, 0.810, 0.677)$ with the variables having their standard definitions (P. A. Ade et al. 2016).

For validation, we instead fix several parameter points and generate many realizations at each point. Specifically, we generated five reference parameter sets, each with lightcone shape (64, 64, 1024), at $(\log_{10} T_{\text{vir}}, \zeta) = (4.699, 30)$, (5.477, 200), (4.8, 131.341), (4.4, 131.341), and (5.6, 19.037). These points were chosen to sample physically distinct regimes within the training domain. Lower values of T_{vir} , associated with lower impact of feedback, allow lower-mass halos to host ionizing sources, increasing the abundance of contributing sources, whereas larger ζ corresponds to more efficient ionizing photon production per collapsed baryon. Thus, the low T_{vir} , high ζ point (4.4, 131.341) represents a regime with relatively abundant and efficient ionizing sources, while the high T_{vir} , low ζ point (5.6, 19.037) represents the opposite limit. The points (4.699, 30) and (5.477, 200) correspond approximately to the ‘‘Faint Galaxy’’ and ‘‘Bright Galaxy’’ benchmark models of B. Greig & A. Mesinger (2017), respectively, and the intermediate point (4.8, 131.341) provides an additional visually structured validation case within the parameter space. For each parameter set, we produced 800 21cmFAST realizations with independent initial conditions. This multi-realization validation design is intended to test not only whether the diffusion model reproduces the central tendency of the signal at fixed parameters, but also whether it learns the conditional diversity of the target distribution.

All reported comparisons below therefore use 800 diffusion samples and 800 21cmFAST samples for each parameter set. To reduce visual crowding in the power-spectrum and scattering-coefficient panels, we focus most figures on three representative validation points: (4.4, 131.341), (5.477, 200), and (4.699, 30). Since all validation points lie within the training range, the present study is an interpolation test rather than an extrapolation test.

Our code supports 2D and 3D input tensors through the same interface:

$$\mathbf{x} \in \mathbb{R}^{H \times Z} \text{ (2D)} \quad \text{or} \quad \mathbf{x} \in \mathbb{R}^{H \times H \times Z} \text{ (3D)}. \quad (2)$$

In this work, $H = 64$ and Z varies by run design, with the most demanding configurations reaching $Z = 1024$.

3.2. Conditional Diffusion Architecture

We use a context-conditioned U-Net (J. Ho et al. 2020; P. Dhariwal & A. Nichol 2021) in which timestep embeddings and condition embeddings are combined in latent space. For the $64 \times 64 \times 1024$ 3D lightcone datasets, the network uses four resolution levels with an anisotropic downsampling and upsampling stride of (2, 2, 4), producing feature resolutions of (64, 64, 1024), (32, 32, 256), (16, 16, 64), and (8, 8, 16). The fiducial comparison architecture uses 128 base channels and channel multipliers (1, 1, 2, 4). We apply one residual block per resolution in the encoder and two residual blocks per resolution in the decoder; additional tests with deeper residual-block configurations are included in the hyperparameter sweep.

The model is dimension agnostic through shared 2D/3D code paths built from Conv{2,3}d in PyTorch, residual blocks, downsampling and upsampling operators, and attention blocks. Attention is applied with four heads at the two lowest spatial resolutions, corresponding to feature maps of (16, 16, 64) and (8, 8, 16) in the 3D case. The timestep embedding dimension is set to 512, corresponding to four times the base channel size. The two astrophysical conditioning parameters are mapped through a linear token embedding of the same dimension, and the condition embedding is added directly to the timestep embedding before it is injected into every residual block.

For all reported experiments, the sampling follows the full denoising diffusion probabilistic model (DDPM) trajectory with 1000 diffusion timesteps and a standard mean-squared-error (MSE) noise-prediction loss (J. Ho et al. 2020). We use the AdamW optimizer with an initial learning rate of 10^{-5} and a cosine-annealing learning-rate decay. For the fiducial 3D runs, each GPU processes 800 lightcones, corresponding to the full training set of 25,600 lightcones distributed across 32 GPUs.

We use a micro-batch size of 2, 120 epochs, and a gradient accumulation of 16, corresponding to a cosine schedule with $T_{\max} = 3000$ optimizer steps. We also tested an exponential moving average (EMA) with a decay rate $\beta = 0.995$ but found no improvement in the reported comparisons; all results shown in this paper therefore exclude EMA.

3.3. Normalization and Dynamic-Range Control

A central empirical finding of this study is that preprocessing dominates training stability at 3D scale. The full preprocessing and postprocessing pipeline is

$$x_{\text{raw}} \rightarrow \text{primary transform} \rightarrow \text{optional squish} \rightarrow \text{diffusion model} \rightarrow \text{inverse squish} \rightarrow \text{inverse transform},$$

where x_{raw} denotes the physical 21 cm brightness-temperature voxel value, and the optional squish step refers to the additional dynamic-range compression defined in Eq. (8). We consider four primary normalization transforms:

1. Yeo–Johnson transform:

$$x' = \text{YJ}(x; \lambda) = \begin{cases} \frac{(x+1)^\lambda - 1}{\lambda}, & \lambda \neq 0, x \geq 0, \\ \log(x+1), & \lambda = 0, x \geq 0, \\ -\frac{(1-x)^{2-\lambda} - 1}{2-\lambda}, & \lambda \neq 2, x < 0, \\ -\log(1-x), & \lambda = 2, x < 0, \end{cases} \quad (3)$$

followed by standardization

$$\tilde{x} = \frac{x' - \mu_{\text{YJ}}}{\sigma_{\text{YJ}}}, \quad (4)$$

where λ is the fitted Yeo–Johnson parameter and $(\mu_{\text{YJ}}, \sigma_{\text{YJ}})$ are the mean and standard deviation of the transformed training distribution.

2. Min–max scaling:

$$\tilde{x} = 2 \frac{x - x_{\min}}{x_{\max} - x_{\min}} - 1, \quad (5)$$

which maps the data to $[-1, 1]$ using fixed dataset-level bounds.

3. Z-score normalization:

$$\tilde{x} = \frac{x - \mu}{\sigma}, \quad (6)$$

with fixed dataset mean μ and standard deviation σ .

4. Arcsinh transform:

$$\tilde{x} = \operatorname{arcsinh}(x). \quad (7)$$

The physical voxel distribution motivates these choices. Most voxels cluster near a brightness temperature of 0 mK; however, there is an additional concentration in the emission phase in positive temperatures, and the absorption tail extends more broadly toward large negative values. This strong skewness makes transformed-space behavior critical: a transform can appear reasonable in transformed space while still producing clear distortions after inversion back to physical units.

After the primary normalization transform, we optionally apply an additional dynamic-range compression step (“squish”) before diffusion training:

$$x_{\text{sq}} = \begin{cases} A \tilde{x}, & k = 0, \\ A \operatorname{arcsinh}(\tilde{x}/k), & k \neq 0. \end{cases} \quad (8)$$

In practice, the main 3D comparisons in this paper use the linear case $k = 0$, so the squish step reduces to a simple amplitude scaling $x_{\text{sq}} = A\tilde{x}$. We tested several amplitude settings and found that $A = 0.1$ provides the most favorable trade-off among the configurations considered here, outperforming both weaker compression ($A = 0.5$, $A = 1$) and overly aggressive compression ($A = 0.01$). Tests with nonlinear squish, such as $(A, k) = (0.1, 1)$, gave behavior similar to the linear $(0.1, 0)$ case. We therefore interpret the main role of the squish stage as controlled dynamic-range compression rather than as a qualitatively new nonlinear transform.

3.4. Evaluation Protocol

We evaluate generated samples against 21cmFAST targets using a hierarchy of complementary diagnostics:

1. brightness-temperature T_b image slices, for direct qualitative inspection;
2. the global signal $\langle T_b \rangle$ versus line-of-sight position or redshift, to test mean evolutionary behavior;
3. the power spectrum, to test two-point spatial structure;
4. reduced scattering coefficients, to test higher-order non-Gaussian morphology (M. Andreux et al. 2020; S. Cheng et al. 2020; B. Greig et al. 2023).

The global signal is the transversely averaged 21 cm brightness temperature as a function of line-of-sight position or redshift. In practice, we first average each

lightcone over the two sky-plane dimensions and then aggregate the resulting curves across 800 realizations using the median. The power spectrum is computed from a square 64×64 two-dimensional lightcone patch spanning one transverse direction and the line of sight, whose starting line-of-sight index corresponds to $z = 11.93$. This redshift was chosen because the global signal, power spectrum, and scattering coefficients are well separated between the representative $(\log_{10} T_{\text{vir}}, \zeta)$ configurations at this stage, making qualitative differences easier to visualize and compare. The resulting statistics are likewise aggregated across realizations using the median. We use the same 64×64 transverse–line-of-sight 2D lightcone patches to compute the reduced second-order scattering coefficients. The second-order scattering coefficients are constructed from cascaded wavelet convolutions followed by modulus operations and spatial averaging. For an input 2D image I , the second-order coefficients can be written as

$$S_2(j_1, \ell_1, j_2, \ell_2) = \langle |I \star \psi_{j_1, \ell_1} \star \psi_{j_2, \ell_2}| \rangle,$$

where $\psi_{j, \ell}$ denotes a wavelet filter at scale j and orientation ℓ , \star denotes convolution, $|\cdot|$ denotes the modulus operation, and $\langle \cdot \rangle$ denotes spatial averaging. These coefficients probe correlations between image structures across different spatial scales and orientations, and therefore provide a compact description of multiscale non-Gaussian morphology. Following X. Zhao et al. (2023), we retain only scale pairs with $j_2 > j_1$, removing redundant scale combinations while preserving the dominant structural information. In practice, we average over the absolute orientation ℓ_1 and retain the relative orientation class $(\ell_2 - \ell_1) \bmod L$, which reduces the number of coefficients while preserving orientation-dependent morphological information. We additionally use logarithmic scattering coefficients for dynamic-range compression, following conventions commonly adopted in prior 2D analyses (X. Zhao et al. 2023).

For the summary-statistic panels in Figures 2, 4, and 5, the shaded bands correspond to the 1σ quantile range estimated from the 800 realizations at fixed parameters. These bands are intended to visualize sample-to-sample diversity at fixed conditioning values rather than formal parameter-estimation uncertainties.

All major diagnostic functions share the same residual definitions:

$$\epsilon_{\text{rel}} = \frac{y_1 - y_0}{|y_0|}, \quad (9)$$

$$\epsilon_{\text{std}} = \frac{y_1 - y_0}{\sigma_0}, \quad (10)$$

$$\epsilon_{\sigma} = \frac{\sigma_1}{\sigma_0} - 1, \quad (11)$$

Table 1. Index-to-hyperparameter mapping used in the hyperparameter-comparison figures. The fiducial configuration is highlighted in bold and serves as the comparison anchor in the sweep. The representative model shown in Figures 3–5 is the corresponding 240-epoch extension (index 12). The *Label* column gives the shorthand labels used in Figures 1 and 2. The final column reports MAE_{std} computed from the global-signal residual channels, which we use as the primary scalar metric for compact comparison across hyperparameter configurations.

Index	Dim	Transform	Amplitude	ResBlocks	Epochs	Label	MAE_{std}
<i>2D transform controls</i>							
1	2D	arcsinh	1	1	120	A1 D2 TAS	7.67
2	2D	min–max	1	1	120	A1 D2 TMM	0.284
3	2D	z-score	1	1	120	A1 D2 TZS	0.338
4	2D	Yeo–Johnson	1	1	120	A1 D2	0.274
<i>3D lightcone runs</i>							
5	3D	min–max	1	1	120	A1 TMM	1.93
6	3D	z-score	1	1	120	A1 TZS	6.35
7	3D	Yeo–Johnson	1	1	120	A1	4.94
8	3D	Yeo–Johnson	0.5	1	120	A0.5	2.80
9	3D	Yeo–Johnson	0.01	1	120	A0.01	1.36
10	3D	Yeo–Johnson	0.1	3	120	RB3	1.20
11	3D	Yeo–Johnson	0.1	2	120	RB2	0.425
12	3D	Yeo–Johnson	0.1	1	240	Ep240	0.272
13	3D	Yeo–Johnson	0.1	1	120	FIDUCIAL	0.389
14	3D	Yeo–Johnson	0.1	1	60	Ep60	1.29
15	3D	Yeo–Johnson	0.1	1	30	Ep30	8.63

where subscripts 0 and 1 denote the reference 21cmFAST ensemble and the generated diffusion-model ensemble, respectively. Here y denotes the ensemble median of the diagnostic quantity under consideration and σ denotes the corresponding ensemble standard deviation. We apply masking thresholds on $|y_0|$ or σ_0 to avoid artificial divergence when the denominator becomes too small. These three channels probe distinct failure modes: ϵ_{rel} measures relative bias with respect to the reference signal, ϵ_{std} measures mismatch relative to the sample variance of the reference ensemble, and ϵ_{σ} measures discrepancies in dispersion. The reported scalar metrics are the mean absolute errors (MAEs),

$$\text{MAE}_{\text{rel}} = \langle |\epsilon_{\text{rel}}| \rangle, \quad (12)$$

$$\text{MAE}_{\text{std}} = \langle |\epsilon_{\text{std}}| \rangle, \quad (13)$$

$$\text{MAE}_{\sigma} = \langle |\epsilon_{\sigma}| \rangle. \quad (14)$$

Among these scalar summaries, we use MAE_{std} as the primary compact ranking metric in the hyperparameter sweep. The reason is pragmatic as well as physical: MAE_{rel} can become numerically unstable when the reference signal is close to zero, while MAE_{σ} is designed specifically to measure recovery of diversity rather than central accuracy. By normalizing the residual to the sample scatter of the reference ensemble, MAE_{std} pro-

vides the most stable single-number measure of conditional bias across the diagnostics considered here. Unless explicitly noted otherwise, our ranking descriptions in the hyperparameter sweep refer to MAE_{std} computed from the global-signal residual channels.

4. RESULTS

4.1. Model Performance Dependence on Preprocessing

We begin with the different preprocessing methods listed in Section 3.3 and the hyperparameter sweep because it provides the clearest quantitative view of which design choices have the largest impact on accuracy. Table 1 lists the indexed runs used in the comparison figures. The fiducial configuration, highlighted in bold, serves as the comparison anchor for the 3D sweep. Figure 1 summarizes the preprocessing and hyperparameter sweep across the 2D and 3D runs. Figure 2 illustrates how these differences appear directly in the global-signal evolution. The representative model shown later in Figures 3–5 is the corresponding 240-epoch extension of that fiducial setup.

Table 1 and Figures 1 and 2 show that the preprocessing and dynamic-range control are the dominant drivers of performance in a 3D setting. The 2D runs serve mainly as control runs for the transforms, while the main scientific comparison is within the 3D model block. In

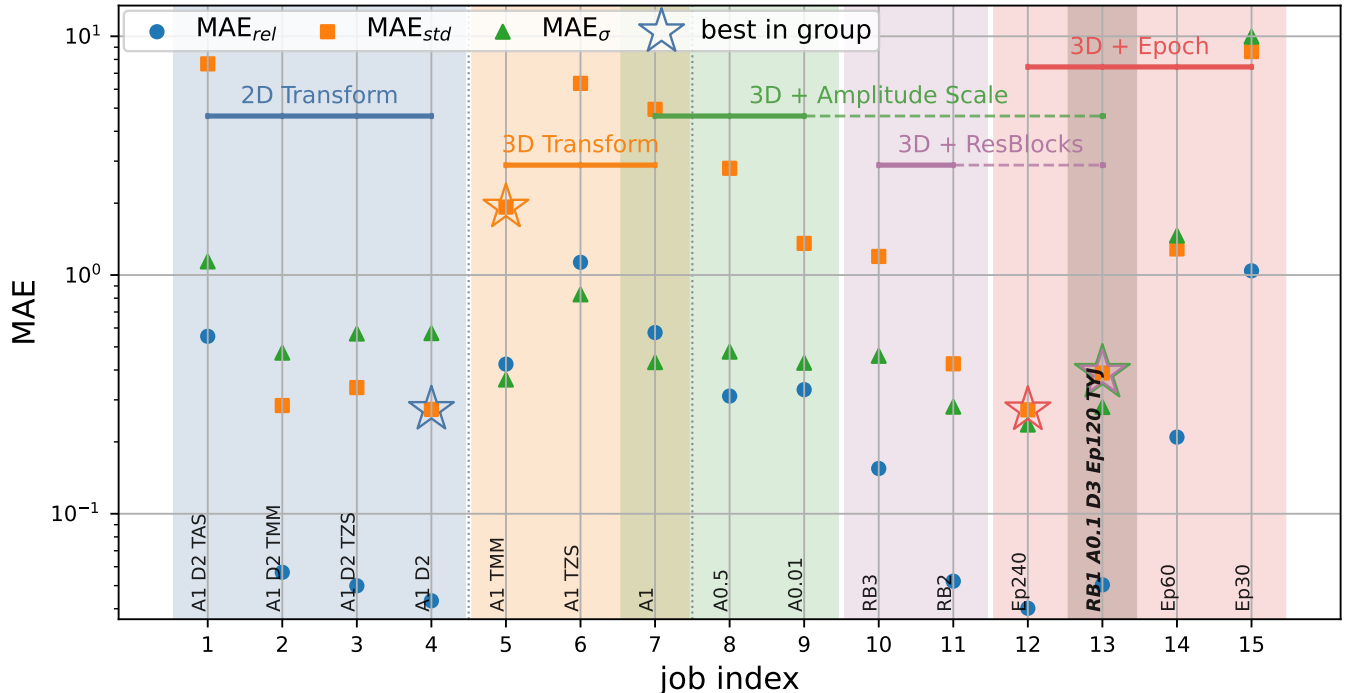


Figure 1. Summary of scalar MAE metrics across the hyperparameter sweep. Markers show MAE_{rel} , MAE_{std} , and MAE_{σ} for each indexed run listed in Table 1 where their labels are given; open stars mark the best run within each comparison group using MAE_{std} as the primary selection metric. The colored guide bands separate the 2D-transform tests, 3D-transform tests, amplitude-scaling tests, residual-block tests, and epoch-length tests.

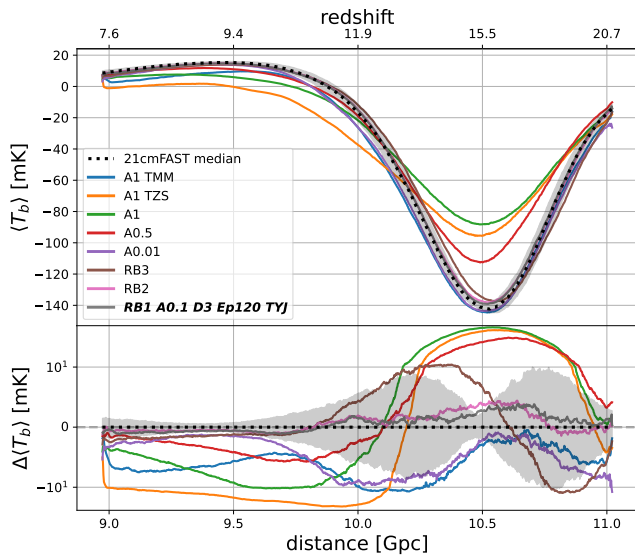


Figure 2. Comparison of selected 3D runs against 21cmFAST (dotted line) using the global signal and its residual, $\Delta(T_b)$. The upper panel shows the median $\langle T_b \rangle$ evolution for representative runs spanning different preprocessing choices, amplitude scalings, and residual-block depths, and the lower panel shows the corresponding deviation from the 21cmFAST median.

the 2D transform tests contained in the blue shaded re-

gion in Figure 1, the Yeo–Johnson and min–max transforms give similarly favorable performance and emerge as the strongest preprocessing choices. Comparing the 2D and 3D transform groups in the same figure shows that the transition from 2D to 3D substantially increases the difficulty of training, with the MAE values rising by roughly an order of magnitude. Within the 3D transform-only subset shown in the orange shaded region of Figure 1, the plain z-score and plain Yeo–Johnson runs perform markedly worse than the min–max transform in the global-signal MAE_{std} ranking. This ordering is then reversed once a moderate amplitude compression is added to the Yeo–Johnson transform, consistent with the interpretation that the plain z-score and plain Yeo–Johnson approaches do not compress the transformed dynamic range strongly enough for the much broader 3D voxel distribution, relative to the 2D cases. The hyperparameter sweep in amplitude A , which are contained in the green shaded region, shows the clearest single trend in the 3D runs: adding an extra compression stage substantially improves performance, and the improvement is not monotonic with compression strength. We find that an intermediate value, $A = 0.1$, performs better than $A = 1, 0.5$, or 0.01 , clearly surpassing the plain min–max baseline.

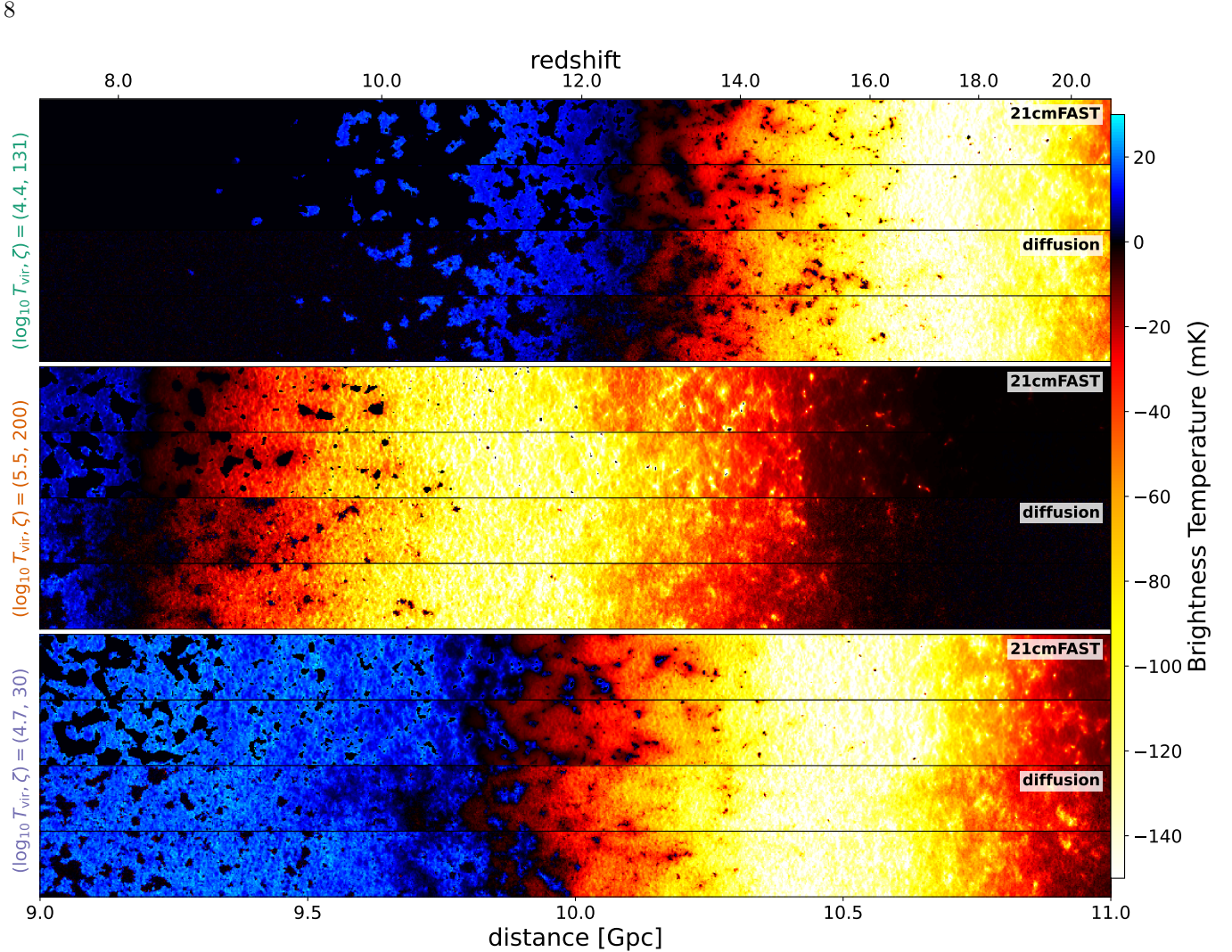


Figure 3. Brightness-temperature slice comparison for the representative 3D run (Yeo–Johnson preprocessing, $A = 0.1$, one residual block per level in the encoder, 240 epochs). For each conditioning point, the upper two strips show independent 21cmFAST realizations and the lower two strips show diffusion-generated realizations.

Figure 2 depicts how these scalar differences appear in the global-signal $\langle T_b \rangle$ evolution itself: preprocessing and dynamic-range control primarily determine whether the absorption trough is placed at the correct depth and redshift, whereas architectural changes such as residual-block depth modulate the remaining mismatch more subtly. In particular, the better-performing compressed Yeo–Johnson runs place the absorption trough closer to the 21cmFAST reference signal in both depth and redshift and remain closest to the reference curve over most of the lightcone, while several alternative settings produce systematic offsets that persist across extended redshift intervals.

The remaining trends are secondary. Figure 1 shows that increasing residual-block depth is not monotonically beneficial: the run with one residual-block (RB1) outperforms the model with two (RB2) and does markedly better than the model with three (RB3),

despite RB3 requiring far greater computational cost (1061-GPU hours for RB3, 536 GPU-hours for RB2, and 347-GPU hours for RB1). This result indicates that simply stacking more parameters does not guarantee better performance for this problem. One plausible interpretation is that, in the small-micro-batch regime enforced by 3D memory limits, the potential representational benefit of additional depth is outweighed by noisier optimization dynamics, so deeper models are not rewarded unless training is already sufficiently stable.

The points in the red shaded region of Figure 1 show a consistent improvement from 30 to 240 epochs, with the 240-epoch run giving the best result among the tested values, although longer training runs were not explored. Owing to computing time and memory constraints, the runs on the left side of the sweep were all trained for 120 epochs. The representative example used in Figures 3–5 corresponds to the 240-epoch configuration.

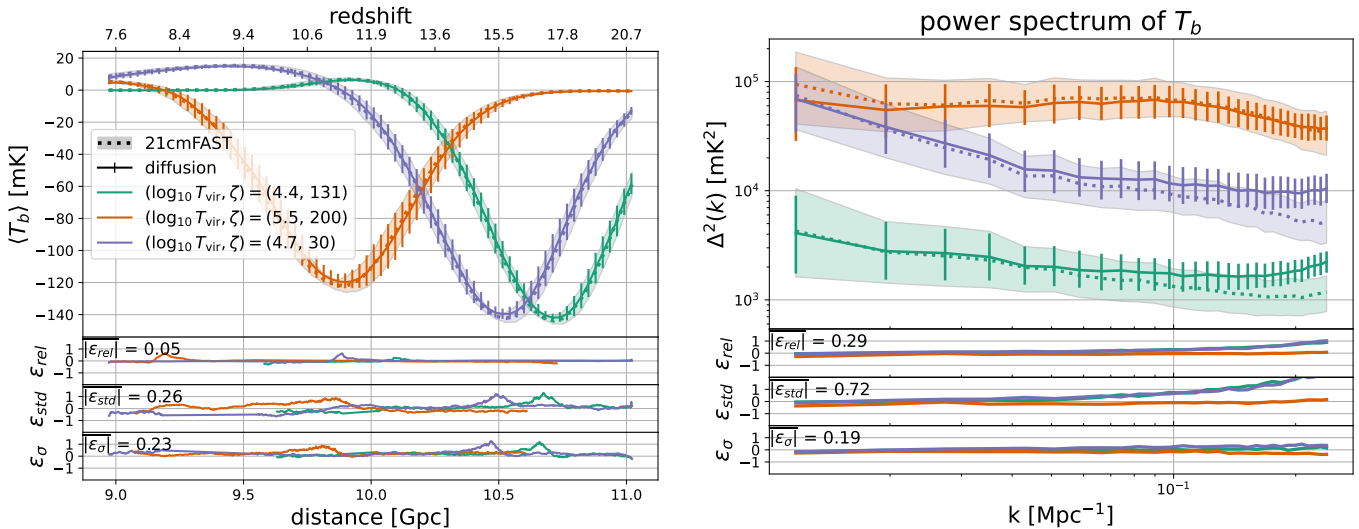


Figure 4. Global-signal (left) and power-spectrum (right) diagnostics for the representative 3D run shown in Figure 3. In both panels, the dashed lines with shaded bands denote the 21cmFAST median and 1σ quantile ranges, while the solid lines with error bars denote the diffusion-model median and 1σ quantile ranges. *Left:* median global signal $\langle T_b \rangle$ as a function of distance/redshift, together with the residual channels ϵ_{rel} , ϵ_{std} , and ϵ_{σ} . *Right:* power-spectrum comparison for the selected transverse–line-of-sight lightcone patches.

Taken together, our hyperparameter sweep supports a narrow but robust conclusion: among the tested configurations, the Yeo–Johnson preprocessing transform combined with a moderate amplitude compression gives the most consistently favorable trade-off between performance and compute time and memory usage, with the strongest direct support coming from the global-signal MAE_{std} ranking.

4.2. Accurately Captured Features in the 3D Model

Having identified a preferred region of hyperparameter space, we now examine the representative extended-training run in more detail. This model uses the same configuration as the fiducial comparison anchor but extends training from 120 to 240 epochs (Table 1, index 12).

The representative run captures the broad large-scale morphology and the main global-signal evolution, but the finer diagnostics show a clear hierarchy of difficulty. Figure 3 provides a qualitative illustration of sample diversity at fixed parameters: for each conditioning point, the upper two strips show two independent 21cmFAST reference realizations and the lower two strips show two corresponding diffusion-generated realizations. The horizontal axis gives comoving distance and the top axis indicates the associated redshift range. The model reproduces the large-scale progression of the brightness-temperature structure along the line of sight, as well as the approximate location and width of the dominant transition region. At the same time, the most visible residuals are local. The generated slices appear

smoother, particularly in ionized bubble-rich regions, they do not always match the sharpest boundaries or fine-scale structure in the reference maps, and they often contain small nonzero pixels within visually dark regions that are cleaner in the 21cmFAST slices. Morphological agreement is therefore stronger on large scales than at the smallest resolved scales, and the sharp separation between low T_b interiors and the surrounding medium is not fully recovered.

Figure 4 shows that this agreement is strongest in the global signal. In both panels, the dashed lines with shaded bands denote the 21cmFAST median and 1σ quantile ranges, while the solid lines with error bars denote the diffusion-model median and 1σ quantile ranges. In the left panel, the model follows the broad timing and depth of the absorption troughs for the three representative parameter choices, with the closest agreement occurring in the large-scale trend. The remaining discrepancies are concentrated near the steepest parts of the evolution, where small shifts in transition location produce visible residual structure. Some residual-channel curves are partially truncated because we mask bins with denominators below 1 mK, thereby avoiding artificial divergence of the ϵ metrics near zero crossings. In the right panel, the generated samples recover the overall ordering and amplitude of $\Delta^2(k)$ across the different parameter settings, but the residual panels show that scale-dependent differences remain, especially toward the highest k modes where the smallest resolved structures are hardest to reproduce accurately. This ordering across diagnostics is physically consistent with

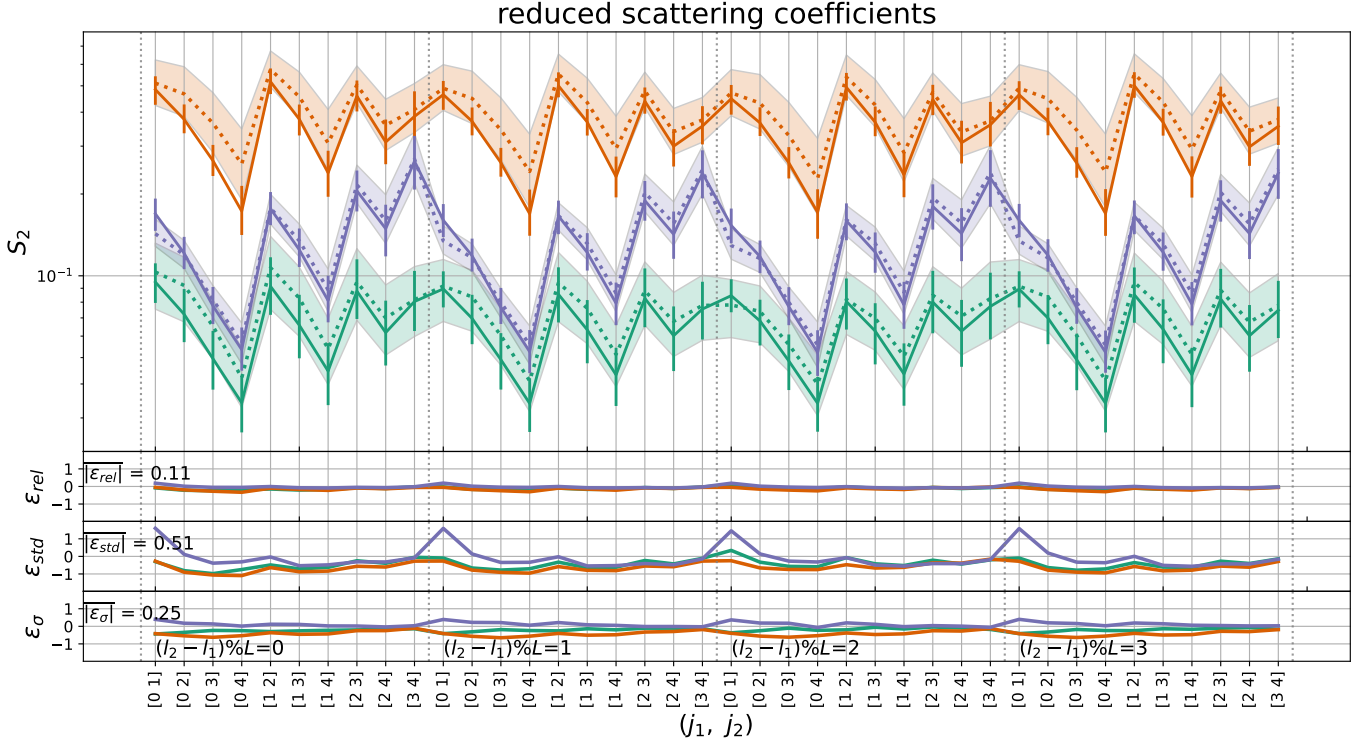


Figure 5. Reduced scattering-coefficient comparison for the representative 3D run shown in Figures 3 and 4. The top panel compares the second-order coefficients S_2 across multiscale index pairs (j_1, j_2) and relative orientation classes, while the lower panels show the corresponding residual channels.

the image-space residuals: once sharp boundaries are smoothed and low T_b interiors are broadened, the largest impact is expected at the smallest resolved scales, even when the large-scale mean evolution is already well captured.

Figure 5 then shows that higher-order morphology remains the most difficult target. The top panel compares the second-order scattering coefficients S_2 across multiscale index pairs (j_1, j_2) and relative orientation classes $(\ell_2 - \ell_1) \bmod L$, while the lower panels report the same three residual channels used elsewhere in the paper. The diffusion outputs track the broad level ordering and oscillatory pattern of the reference coefficients, indicating that the model captures a substantial fraction of the non-Gaussian morphological information present in the lightcone patches. At the same time, the residual structure shows that higher-order statistics remain more difficult to match than the global signal, so even visually plausible samples can retain measurable errors in multiscale morphology. The main positive result of the representative run is therefore not perfect agreement, but a structured and interpretable level of success across diagnostics.

4.3. Inaccuracies in the Preferred Model

To isolate the remaining failure modes more directly, Figure 6 compares voxel value probability density functions in both transformed space and raw space, which shows that an important part of the difficulty already appears in transformed voxel space. The two panels show voxel value probability density functions in transformed space (left) and raw brightness temperature T_b space (right) for 21cmFAST targets and diffusion-generated samples, respectively. The main challenge is the strong concentration of voxels near 0 mK in the physical lightcone distribution: the reference data contain a sharply peaked, nearly delta-function-like near-zero component, whereas the diffusion model reproduces this feature only as a peak with finite width. Although some preprocessing choices place the dominant near-zero peak at roughly the correct location, the diffusion model does not fully recover its height, width, or surrounding distribution. In transformed voxel space, min-max performs better than plain z-score and plain Yeo-Johnson because it compresses the data into a narrower range, making the target distribution easier for the diffusion model to reproduce. This observation helps explain why a secondary squish step can improve 3D training: it further

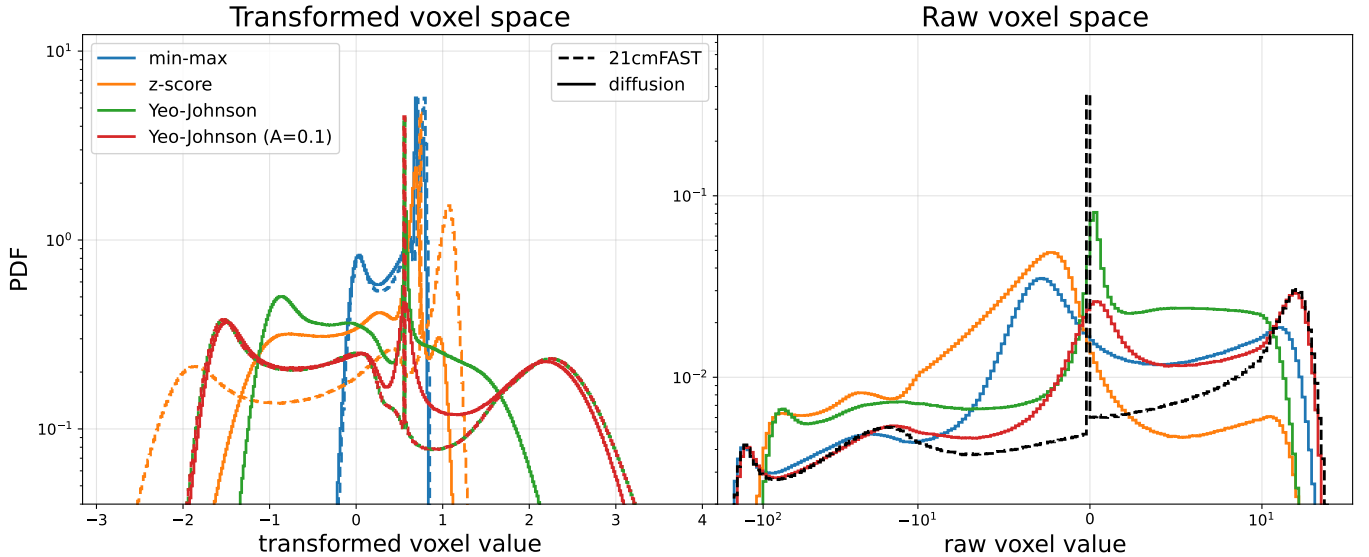


Figure 6. Comparison of preprocessing choices using lightcone voxel value distributions. The two panels show voxel value probability density functions in transformed space (left) and raw brightness-temperature space (right) for 21cmFAST targets and diffusion-generated samples.

narrows the transformed dynamic range that the diffusion model must learn.

The same figure also clarifies why transformed-space improvement is not the whole story. A Yeo–Johnson transform followed by an additional amplitude compression with $A = 0.1$ yields the best overall agreement in both transformed and raw space, substantially improving upon the case without the additional compression. After mapping the samples back to physical brightness-temperature space, however, the near-zero component remains visibly broader than in the 21cmFAST targets, indicating that the model still does not perfectly match this part of the distribution. In the 21cmFAST reference, the near-zero voxel population is sharply concentrated and nearly delta function-like, whereas the diffusion model broadens it into a finite-width distribution. After inversion back to raw brightness-temperature space, voxel values that should remain tightly clustered near 0 mK are instead spread over a continuous range, including small positive and negative values. In image space, this broadening manifests as visually dark regions that are less cleanly separated from their surroundings, with small nonzero pixels appearing inside regions that are closer to zero in the reference maps. This interpretation is consistent with the local residuals seen in Figure 3, and it also provides a plausible link to the residual power-spectrum mismatch at high k : once low T_b interiors and sharp boundaries are smeared into a broader continuum, the resulting fields naturally lose some of the smallest-scale contrast even if the large-scale trend is preserved.

Together with Figure 2, the voxel-PDF comparison also shows why a voxel-level agreement alone is not sufficient to identify a preferred preprocessing strategy. Min–max is relatively competitive in the voxel-PDF comparison, but its global-signal behavior remains systematically biased, with the median brightness-temperature curve consistently shifted below the 21cmFAST reference over much of the lightcone evolution. This behavior is consistent with the strong skewness of the voxel distribution: although min–max scaling preserves the overall range, it does not sufficiently regularize the highly asymmetric near-zero population, leading the diffusion model to underestimate the brightness temperature after inversion back to physical units. In contrast, the better compressed Yeo–Johnson runs yield a more favorable compromise across voxel level and global signal diagnostics: the reconstructed median fluctuates around the 21cmFAST reference while remaining largely within the reference 1σ band throughout most of the lightcone evolution. Overall, Figure 6 shows that preprocessing plays a major role in voxel-level fidelity: additional dynamic-range compression improves the agreement, but does not fully eliminate the difficulty of reproducing the sharply concentrated near-zero voxel population. The preferred configuration should therefore be understood not as universally optimal across every metric, but as the most consistent trade-off among the tested configurations.

5. DISCUSSION

5.1. *Challenges in 3D Lightcone Emulation*

The move from 2D image generation to 3D lightcone emulation is not simply a dimensional upgrade. The dominant failure modes in our experiments arise from coupled computational and statistical effects: memory constraints force small micro-batches, small batches amplify optimization noise, and unstable normalization magnifies the resulting errors. In this regime, preprocessing is not a minor implementation detail but a principal modeling choice.

Our results also show that evaluation must be physically layered. The global signal, power spectrum, and scattering coefficients probe distinct aspects of fidelity: mean evolution, two-point structure, and higher-order non-Gaussian morphology. This hierarchy matters for 21 cm lightcones because their information content is not fully described by Gaussian statistics. A model may therefore appear satisfactory under visual inspection or even under low-order summaries while still retaining meaningful biases in morphology-sensitive diagnostics. That is precisely why the scattering transform is useful here: it helps expose discrepancies that would be missed by image inspection or by the global signal alone, consistent with the broader conclusions of [X. Zhao et al. \(2023\)](#). More broadly, our results argue that future 21 cm generative-emulator studies should not rely on visual inspection alone, and should include morphology-sensitive validation in addition to lower-order summaries whenever the scientific goal depends on preserving non-Gaussian structure.

The validation design also allows a more specific statement about diversity. Because the reference sets contain many independent realizations at fixed parameter points, they test whether the model learns a distribution rather than only a deterministic mean mapping. The dispersion metric MAE_σ suggests that the better-performing 3D models recover the conditional spread of the signal reasonably well, even when some residual biases remain in lower-order or higher-order summary statistics. This is encouraging for inference-oriented applications, where realistic sample diversity is essential.

5.2. *Limitations and Future Work*

This paper focuses on emulator fidelity under simulation-level conditions rather than a complete survey-facing inference pipeline. Several ingredients remain necessary for that next step: instrument response and foreground contamination, uncertainty calibration beyond percentile envelopes, larger controlled studies of realization-to-realization variance, and direct downstream validation in simulation-based inference (SBI)

or Markov chain Monte Carlo (MCMC) workflows. One specific open question is whether the small-scale smoothing identified in [Sections 4.2 and 4.3](#) would lead to measurable parameter-level bias in downstream inference. Quantifying that effect will require explicit SBI or MCMC tests and is beyond the scope of this paper. The present work should therefore be viewed as a baseline study of generative fidelity rather than as a complete end-to-end inference demonstration.

The present validation is also interpolative: all reference parameter points lie within the training range. In addition, the training data use one lightcone per training parameter pair, whereas the validation ensembles use many realizations at fixed parameter points. This design is efficient for parameter-space coverage, but future work could explore denser multi-realization training sets, wider astrophysical conditioning spaces, and more explicit tests of generalization under distribution shift. Finally, although the present analysis uses 800-sample ensembles for both the generated and reference sets, more extensive sampling studies could still be valuable for tightening uncertainty estimates.

More broadly, the main astrophysical value of this work lies in methodology and benchmarking. Before a 3D generative emulator can be trusted for survey-facing 21 cm inference, it must be validated in a way that is sensitive not only to image appearance but also to the physically meaningful statistics of the signal. The present study identifies preprocessing and diagnostic choices that materially affect that trustworthiness and therefore helps define a more robust baseline for future emulator development.

6. CONCLUSION

We have presented a study of conditional diffusion modeling for 3D 21 cm lightcone emulation. The main conclusion is methodological: in this high-dimensional regime, stable and physically meaningful generation depends primarily on preprocessing and dynamic-range control, with architecture depth and training duration becoming secondary once optimization has been stabilized. Our diagnostics further show that visual plausibility is not enough; physically motivated summaries are needed to assess emulator quality.

Among the tested configurations, Yeo–Johnson preprocessing with moderate amplitude compression provides the most consistently favorable trade-off, with the clearest quantitative support coming from the global-signal MAE_{std} ranking and with qualitatively compatible behavior in the complementary diagnostics. At the same time, the hierarchy of diagnostics shows that success is easier to achieve in the global signal than in

the power spectrum or scattering coefficients, so visually convincing outputs can still retain measurable physical biases. In particular, the broadened near-zero voxel component, the corresponding smoothing of low T_b regions in image space, and the residual mismatch at the smallest resolved scales all point to the same limitation: recovering the full small-scale and morphology-sensitive structure of the 3D lightcone distribution remains harder than matching its large-scale evolution.

The present work therefore provides a reproducible simulation-level baseline for judging 3D 21 cm lightcone emulators in terms of mean evolution, two-point structure, and higher-order morphology. More broadly, it argues that future 21 cm emulator studies should move beyond visual inspection and global signals alone and include morphology-sensitive validation when assessing physical fidelity, especially if the intended application is inference rather than image generation.

ACKNOWLEDGMENTS

We acknowledge funding support from a Georgia Tech Research Institute IRAD award, NSF grants AST-2108020 and AST-2510197, and NASA grant 80NSSC21K1053. This research used resources of the National Energy Research Scientific Computing Center (NERSC), a U.S. Department of Energy Office of Science User Facility, through the GenAI@NERSC award.

DATA AVAILABILITY

The training and validation data underlying this article are available from the corresponding author upon request. The code used for the analysis and model development is publicly available at <https://github.com/Xsmos/ml21cm>.

Software: 21cmFAST (A. Mesinger et al. 2011; B. Greig & A. Mesinger 2018), PyTorch (A. Paszke et al. 2019), NumPy (C. R. Harris et al. 2020), Matplotlib (J. D. Hunter 2007)

APPENDIX

A. IMPLEMENTATION DETAILS FOR REPRODUCIBILITY

A.1. Architecture and Diffusion Settings

The main architectural configuration is summarized in Section 3.2. Here we record only the implementation details most relevant for reproducibility.

In `ContextUnet`, 2D and 3D are unified through dimension-dependent convolution and resampling operators. The residual block uses the GroupNorm-based normalization (32 groups), SiLU-style nonlinearity, a 3×3 convolution, timestep-conditioned embedding injection, dropout, and a final zero-initialized convolution, together with a residual skip connection. Depending on the configuration, the skip path is identity, 1×1 , or 3×3 . When upsampling or downsampling is requested inside the residual block, the feature path and skip path are resampled in parallel before the final convolution.

The attention block normalizes the feature tensor, projects it to query, key, and value tensors with a 1×1 convolution in flattened spatial coordinates, applies scaled dot-product attention, and returns the result through a residual connection.

In `training/diffusion.py` provided in our GitHub repository, the DDPM training uses the following settings:

1. `betas=(1e-4, 0.02)` with a linear schedule,
2. `num_timesteps=1000`,

3. MSE loss on predicted noise,
4. AdamW optimizer with an initial learning rate of 10^{-5} ,
5. cosine annealing learning-rate schedule, and
6. gradient clipping (`max_norm=1.0`).

We also tested an exponential moving average (EMA) with a decay rate $\beta = 0.995$ but found no improvement in the final comparisons, therefore the reported results do not use EMA.

A.2. Data Pipeline and Normalization

For each sample, the loader returns an image tensor and a normalized condition vector:

$$(\mathbf{x}, \mathbf{c}), \quad \mathbf{c} \in [0, 1]^2, \quad (\text{A1})$$

where \mathbf{c} corresponds to $(\log_{10} T_{\text{vir}}, \zeta)$ after min-max rescaling. Let \mathbf{x} denote a raw voxel value of the 21 cm brightness-temperature field. Image-space preprocessing is selected via `scale_path` and uses the four normalization choices listed in Section 3.3. After the primary normalization step, the training code can additionally apply the squish transform

$$x_{\text{sq}} = \begin{cases} A \tilde{x} & (k = 0) \\ A \operatorname{arcsinh}(\tilde{x}/k) & (k \neq 0) \end{cases} \quad (\text{A2})$$

with an inverse mapping applied after sampling to recover the physical brightness-temperature space. In the main 3D comparisons, the fiducial setting uses the linear case $(A, k) = (0.1, 0)$.

A.3. Stability and Memory Controls for 3D

The dimensional expansion from 2D to 3D required several explicit controls for training stability and memory efficiency, including distributed data parallel execution, automatic mixed precision, gradient accumulation, optional checkpointed U-Net blocks, and anisotropic downsampling choices tailored to the line-of-sight direction. The reported 3D runs were trained on 32 NVIDIA

A100 GPUs with 80 GB of device memory, and even at that memory scale the full-resolution $64 \times 64 \times 1024$ setup remained constrained to very small micro-batches. In the fiducial 3D setup, each GPU processes 800 lightcones, corresponding to the full training set of 25,600 lightcones distributed across 32 GPUs. We use a micro-batch size of 2, gradient accumulation of 16, and an additional amplitude-compression step $\text{squish}(0.1, 0)$, with training carried out for 120 epochs. These settings correspond to a cosine learning-rate schedule with $T_{\max} = 3000$ optimizer steps. The anisotropic stride design is particularly important in 3D because it reduces memory usage while remaining better matched to the elongated lightcone geometry along the line of sight.

REFERENCES

- Abdurashidova, Z., Aguirre, J. E., Alexander, P., et al. 2022a, *ApJ*, 925, 221, doi: [10.3847/1538-4357/ac1c78](https://doi.org/10.3847/1538-4357/ac1c78)
- Abdurashidova, Z., Aguirre, J. E., Alexander, P., et al. 2022b, *ApJ*, 924, 51, doi: [10.3847/1538-4357/ac2ffc](https://doi.org/10.3847/1538-4357/ac2ffc)
- Ade, P. A., Aghanim, N., Arnaud, M., et al. 2016, *Astronomy & Astrophysics*, 594, A13
- Andreux, M., Angles, T., Exarchakis, G., et al. 2020, *Journal of Machine Learning Research*, 21, 1
- Andrianomena, S., Villaescusa-Navarro, F., & Hassan, S. 2022, arXiv e-prints, arXiv:2211.05000, doi: [10.48550/arXiv.2211.05000](https://doi.org/10.48550/arXiv.2211.05000)
- Barkana, R., & Loeb, A. 2001, *PhR*, 349, 125, doi: [10.1016/S0370-1573\(01\)00019-9](https://doi.org/10.1016/S0370-1573(01)00019-9)
- Cheng, S., Ting, Y.-S., M é nard, B., & Bruna, J. 2020, *Monthly Notices of the Royal Astronomical Society*, 499, 5902, doi: [10.1093/mnras/staa3165](https://doi.org/10.1093/mnras/staa3165)
- DeBoer, D. R., Parsons, A. R., Aguirre, J. E., et al. 2017, *PASP*, 129, 045001, doi: [10.1088/1538-3873/129/974/045001](https://doi.org/10.1088/1538-3873/129/974/045001)
- Dhariwal, P., & Nichol, A. 2021, *Advances in neural information processing systems*, 34, 8780
- Diao, K., & Mao, Y. 2023, arXiv e-prints, arXiv:2307.04976, doi: [10.48550/arXiv.2307.04976](https://doi.org/10.48550/arXiv.2307.04976)
- Diao, K., & Mao, Y. 2025, *ApJ*, 992, 173, doi: [10.3847/1538-4357/ae0325](https://doi.org/10.3847/1538-4357/ae0325)
- Furlanetto, S. R., Oh, S. P., & Briggs, F. H. 2006, *Physics reports*, 433, 181
- Gagnon-Hartman, S., Cui, Y., Liu, A., & Ravanbakhsh, S. 2021, *Monthly Notices of the Royal Astronomical Society*, 504, 4716, doi: [10.1093/mnras/stab1158](https://doi.org/10.1093/mnras/stab1158)
- Goodfellow, I. J., Pouget-Abadie, J., Mirza, M., et al. 2014, arXiv e-prints, arXiv:1406.2661, doi: [10.48550/arXiv.1406.2661](https://doi.org/10.48550/arXiv.1406.2661)
- Greig, B., & Mesinger, A. 2017, *Proceedings of the International Astronomical Union*, 12, 1821, doi: [10.1017/S1743921317011103](https://doi.org/10.1017/S1743921317011103)
- Greig, B., & Mesinger, A. 2018, *MNRAS*, 477, 3217, doi: [10.1093/mnras/sty796](https://doi.org/10.1093/mnras/sty796)
- Greig, B., Ting, Y.-S., & Kaurov, A. A. 2023, *MNRAS*, 519, 5288, doi: [10.1093/mnras/stac3822](https://doi.org/10.1093/mnras/stac3822)
- Harris, C. R., Millman, K. J., van der Walt, S. J., et al. 2020, *Nature*, 585, 357, doi: [10.1038/s41586-020-2649-2](https://doi.org/10.1038/s41586-020-2649-2)
- Ho, J., Jain, A., & Abbeel, P. 2020, *Advances in neural information processing systems*, 33, 6840
- Hothi, I., Allys, E., Semelin, B., & Meriot, R. 2026, *A&A*, 706, A15, doi: [10.1051/0004-6361/202555896](https://doi.org/10.1051/0004-6361/202555896)
- Hunter, J. D. 2007, *Computing in Science & Engineering*, 9, 90, doi: [10.1109/MCSE.2007.55](https://doi.org/10.1109/MCSE.2007.55)
- Koopmans, L., Pritchard, J., Mellema, G., et al. 2015, *SKA Organisation*, Manchester, 1
- List, F., & Lewis, G. F. 2020, *Monthly Notices of the Royal Astronomical Society*, 493, 5913, doi: [10.1093/mnras/staa523](https://doi.org/10.1093/mnras/staa523)
- Mesinger, A., Furlanetto, S., & Cen, R. 2011, *MNRAS*, 411, 955, doi: [10.1111/j.1365-2966.2010.17731.x](https://doi.org/10.1111/j.1365-2966.2010.17731.x)
- Morales, M. F., & Wyithe, J. S. B. 2010, *ARA&A*, 48, 127, doi: [10.1146/annurev-astro-081309-130936](https://doi.org/10.1146/annurev-astro-081309-130936)
- Paszke, A., Gross, S., Massa, F., et al. 2019, in *Advances in Neural Information Processing Systems 32*
- Prelogović, D., & Mesinger, A. 2024, *A&A*, 688, A199, doi: [10.1051/0004-6361/202449309](https://doi.org/10.1051/0004-6361/202449309)
- Prelogović, D., Mesinger, A., Murray, S., Fiameni, G., & Gillet, N. 2021, *Monthly Notices of the Royal Astronomical Society*, 509, 3852, doi: [10.1093/mnras/stab3215](https://doi.org/10.1093/mnras/stab3215)
- Pritchard, J. R., & Loeb, A. 2012, *Reports on Progress in Physics*, 75, 086901

- Rouhiainen, A., Münchmeyer, M., Shiu, G., Gira, M., & Lee, K. 2024, *PhRvD*, 109, 123536, doi: [10.1103/PhysRevD.109.123536](https://doi.org/10.1103/PhysRevD.109.123536)
- Tingay, S. J., Goeke, R., Bowman, J. D., et al. 2013, *PASA*, 30, e007, doi: [10.1017/pasa.2012.007](https://doi.org/10.1017/pasa.2012.007)
- van Haarlem, M. P., Wise, M. W., Gunst, A. W., et al. 2013, *A&A*, 556, A2, doi: [10.1051/0004-6361/201220873](https://doi.org/10.1051/0004-6361/201220873)
- Villanueva-Domingo, P., & Villaescusa-Navarro, F. 2021, *ApJ*, 907, 44, doi: [10.3847/1538-4357/abd245](https://doi.org/10.3847/1538-4357/abd245)
- Zhao, X., Mao, Y., Cheng, C., & Wandelt, B. D. 2022, *The Astrophysical Journal*, 926, 151, doi: [10.3847/1538-4357/ac457d](https://doi.org/10.3847/1538-4357/ac457d)
- Zhao, X., Mao, Y., Zuo, S., & Wandelt, B. D. 2024, *ApJ*, 973, 41, doi: [10.3847/1538-4357/ad5ff0](https://doi.org/10.3847/1538-4357/ad5ff0)
- Zhao, X., Ting, Y.-S., Diao, K., & Mao, Y. 2023, *Monthly Notices of the Royal Astronomical Society*, 526, 1699